Comput. Biol. Med. Vol. 22, No. 5, pp. 305–323, 1992
Printed in Great Britain

0010-4825/92 $5.00+.00

A COMPUTER MODEL FOR THE STUDY OF ELECTRICAL CURRENT FLOW IN THE HUMAN THORAX

CHRISTOPHER R. JOHNSON, ROBERT S. MACLEOD and PHILIP R. ERSHLER
Nora Eccles Harrison Cardiovascular Research and Training Institute, University of Utah, Salt Lake City, UT 84112, U.S.A.

(*Received* 25 *November* 1991; *received for publication* 1 *May* 1992)

Abstract—Electrocardiography has played an important role in the detection and characterization of heart function, both in normal and abnormal states. In this paper we present an inhomogeneous, anisotropic computer model of the human thorax for use in electrocardiography with emphasis on the calculation of transthoracic potential and current distributions. Knowledge of the current pathways in the thorax has many applications in electrocardiography and has direct utility in studies pertaining to cardiac defibrillation, forward and inverse problems, impedance tomography, and electrode placement in electrocardiography.

Anisotropic Computer simulation Finite element method
Forward solution Inhomogeneous Transthoracic current Visualization

INTRODUCTION

An important problem in the biophysical study of electrocardiography is the determination of the pathways of current flow through the body due to cardiac current sources. The knowledge of this current can be applied in many different aspects of electrocardiology, including studies relating to defibrillation, forward and inverse problems, impedance techniques, lead field theory, and electrode placement. Furthermore, the relationship between potential and current distributions in the thorax has implications for biophysical studies outside of electrocardiology, most notably the biological effects of electromagnetic fields on the human body.

In an intact volume conductor current cannot be measured directly and so must be derived from the distribution of electric potential given the local geometric and conductive properties of the medium. Likewise, electric potential can be practically measured only on the surface of the intact volume conductor. Potential distribution within the volume can, however, be predicted from surface measurements providing the geometry and electrical properties of the medium enclosed by the bounding surface(s) are known in sufficient detail. This report describes just such a mathematical model, which includes an explicit, magnetic resonance image based geometrical description of the human thorax and utilizes the finite element method to solve for both potential and current distributions.

The utility of such a model is many-fold. Perhaps its foremost importance to the field of clinical cardiology will be the design of defibrillators, both external and implantable, since efficient and reliable design requires an understanding of current flow in the human thorax. While defibrillation has been an effective clinical tool for many years, the fundamental knowledge of the mechanism that ends the rhythm disorder is still unknown. While some propose that only a critical mass of myocardium must be depolarized [1] and others argue that one must achieve a sufficient current density throughout the myocardium [2], Crampton noted that, "... it is clear that the inability to access the correct transthoracic current pathway is the most common reason for failure to

terminate the rhythm disorder" [3]. One possible reason for this inability is that, until now, there has not been a complete enough model to simulate realistic situations in humans. In early defibrillation modeling studies, Claydon *et al.* calculated cardiac surface potentials from body surface potentials resulting from different stimulation–electrode configurations. Their geometric model was a three-dimensional homogeneous canine thorax [4]. In a more recent study Sepulveda *et al.* calculated myocardial potential and current densities in a two-dimensional isotropic, inhomogeneous canine cross-section [5]. In terms of human models, only the model of Ahmed *et al.*, attempted to calculate three-dimensional currents. Their model, however, was restricted to a partial thorax due to the limited capacity of the commercial software package they utilized [6]. None of the above models explicitly included anisotropy, nor the geometrical complexity associated with actual human data.

A basic physiological application of such models is to aid our understanding of how the normal current pathways generated by cardiac sources manifest themselves in space and time. The flow of electric current in the human thorax originates in electrical activation and recovery of cardiac tissue. Activation of cardiac muscle is the process by which cells undergo rapid depolarization resulting in a propagation of excitation waves moving through the myocardium at approximately 0.5–2 m/sec (depending on tissue type) [7]. This excitation wavefront can be thought of as a distributed surface of current dipoles or source–sink pairs with a separation distance of the order of a millimeter. During the depolarization process this excitation wave produces an extracellular potential field Φ, which depends on the intensity of the cardiac membrane current, the distance from and orientation of the source–sink pair, and the geometry and conductivity of the inhomogeneous volume within the thorax. Recovery of the cardiac membrane is characterized by a return to the polarized resting state.

Associated with the flow of current due to both activation and recovery is the appearance of electric potential distributions on and within the human thorax. These time-varying potentials, can be measured invasively as epicardial electrograms and when measured on the body surface, are known as electrocardiograms. It is possible to compute the transthoracic currents that are associated with cardiac electrical activity, either directly from epicardial potentials (forward solution) or indirectly from body surface potentials (inverse solution). Another form of the forward solution is to calculate thoracic currents which arise due to the application of defibrillatory stimuli, both externally, and via implantable defibrillators. The requirements for an accurate representation of the current flow in a human torso include effective numerical techniques, a detailed geometrical description of the thorax, including internal structures, the conductivities of the tissues, and a means of expressing cardiac electrical activity in terms of epicardial potentials.

The focus of virtually all previous studies of cardiac bioelectric phenomena in the torso has been the dependence of body surface potentials on cardiac sources (forward solution) [8, 9] or, the reverse, determining cardiac sources from body surface potentials (inverse solution) [10–17]. These studies have often ignored the actual calculation of the volume currents, and most have omitted some aspect of the complexity of the problem, particularly inhomogeneity and anisotropy of the volume conductor.

Previous studies [18], suggest that a rigorous treatment for electrocardiographic applications requires that the intravacitary blood mass, skeletal muscle, lungs, and subcutaneous fat, each with appropriate values of conductivity, be included. These tissues have average relative bulk conductivities of approximately 15:10:2:1 respectively. While biological tissue is neither homogeneous nor isotropic at the microscopic level, at the macroscopic level most tissue can be treated as such. The major exception is that of skeletal muscle, whose striated structure causes the relationship between the electric field and current vectors to vary with the orientation of the muscle, in other words, the tissue displays anisotropy. Thus, for striated muscle, even at a macroscopic level, the conductivity cannot be expressed as a simple, bulk value but must be represented as a quantity which depends on direction. This can be accomplished

mathematically by representing the muscle conductivity as a tensor that varies spatially, depending on local fiber orientation.

The results we describe here indicate that transthoracic currents can be calculated in a realistic model of the human thorax and that, relative to previous work, inclusion of anisotropic inhomogeneity, increased geometric resolution, and improved numerical techniques enhance—and may be necessary for—accurate calculation of these currents.

The software that has been developed for calculating transthoracic current includes: (1) programs to construct, manipulate, and display large scale, three-dimensional geometric models, (2) a three-dimensional finite element program to solve the electrocardiographic field equation in its most general form (i.e. one fully capable of incorporating anisotropic inhomogeneities and a wide variety of potential and current sources), (3) an algorithm with which we can apply a general set of boundary conditions for use with various experimental and simulation conditions, such as injection of external or internal defibrillation currents, and (4) programs which solve the large system of equations for the current flow and potential distributions and display them graphically. (See the Appendix for a more complete listing of the software.)

The geometric basis of these computations is a discrete, three-dimensional model of an actual human torso, including inhomogeneous regions and, where appropriate, assignment of their anisotropic nature. To this end, we have performed complete thoracic MRI scans on several subjects and, from one of these subjects, have constructed two geometric models at different spatial resolutions. Conductivities have been assigned to each individual volume element in the models based on values from the literature. The model we have developed is ideal for simulating electrocardiograms and the current pathways resulting from both normal and abnormal cardiac electrical activity as well as for estimating transthoracic current pathways which arise due to defibrillatory current pulses.

METHODS

Model construction

Although there exist no known "minimum requirements" for calculating thoracic potentials and currents, studies by other investigators [14–17] indicate that accurate rendition of the geometry to which the forward solution is applied is required in order to generate realistic estimates. In fact our aim in future studies, is to examine the issue of spatial resolution as well as the effect of anisotropic inhomogeneities on computed thoracic distributions. Hence, one goal of this study was to develop the tools with which to create models that are both as accurate and highly resolved as possible, yet which remain computationally rational.

The most exact method of performing three-dimensional reconstruction in humans, without subjecting them to unacceptable radiation, is by means of magnetic resonance imaging (MRI) techniques. All MRI imaging for this study was done at a step size of 5 mm, from just below the umbilicus to just below the chin (typically 50–70 cm). Before the tomography was begun, a set of 192 mineral oil-filled phantom electrodes were applied to the subject according to the standard procedure for 192-lead body surface mapping [19, 20]. Mineral oil appears opaque in MRI images and can be used to locate the electrode positions. An example of a single layer of an MRI scan, which includes the heart, lungs, and muscle and fat layers is shown in Fig. 1a.

While magnetic resonance tomographic images provide the basis for reconstruction of the geometry required for forward and inverse calculations, further manipulation is required before this geometry is available for computations. Processing consisted of extracting, from the 100–140 slices of image data, the location and shape of the major surfaces within the thorax: body surface, subcutaneous fat, skeletal muscle, lungs, and epicardium. The volumes within each of these surfaces was then discretized into tetrahedral elements and assigned realistic conductivity values. The surfaces themselves were also tessellated into triangular elements and used both for model computations and for subsequent graphical display of the results.

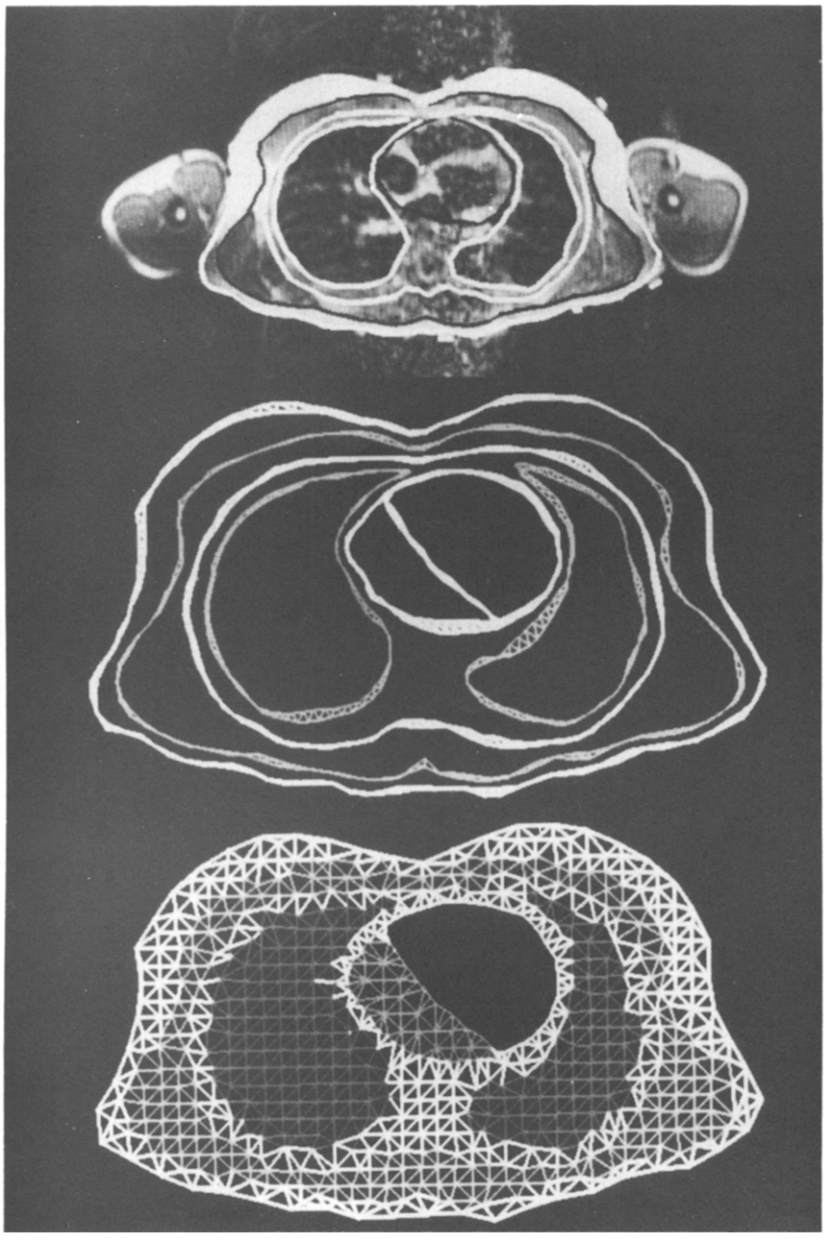

Fig. 1. An example of construction of a single slice of the torso model, starting in the top panel with (a) the magnetic resonance image (NMR) of a single layer. The view perspective is caudal to cranial, with the anterior surface at the top of each panel. Solid black and white lines outline the various surfaces to be incorporated into the model. The middle panel, (b), shows the same layer as in panel (a), now combined with its neighboring layer to form a three-dimensional slice, with each surface digitized, smoothed and triangulated. The bottom panel, (c), contains the same slice again, with added grid points, tessellated into tetrahedral volume elements. Each element is assigned a different conductivity based on its location within the slice. The different shades of gray indicate the main tissue groups, fat, skeletal muscle, lungs, a bulk conductivity value assigned to all regions that fell outside of the rest, and the atrial region of the heart.

In the first step of this procedure, the output from the MRI system was transferred first via digital magnetic tape, then over a local area computer network, to a Macintosh II computer on which individual layers were displayed and the surfaces manually digitized [21]. The sampled points ("raw layer data") from all the surfaces were then transferred to a DEC VAX 4000 computer and a Silicon Graphics Iris 4D/210 VGX workstation for further refinement.

In order to establish uniform spacing of the points defining the surfaces, we interpolated the raw layer data using a parametric cubic-spline algorithm programmed for this application. The value of point separation set in the interpolation program depended on the complexity (curvature) of the individual layer being processed and typically ranged from 3 to 10 mm. Points from pairs of successive layers of the same surface were then combined into "slices"; that is, they represented volumes and not just planar layers. The points in these slices were then connected to form triangles which defined the outer surface of a tissue region in the slice. We have written triangularization programs which use local nearest-neighbor criteria and the fact that spacing between layers was uniform to construct triangles that were as close to equilateral as possible. The triangulated slices occasionally required some manual editing, which we performed using an Evans and Sutherland PS390 graphics system connected to the Vax 4000, and the IRIS 4D/210 graphics workstation. A sorting program then produced complete descriptions of each surface containing the points and triangle connectivities from all slices that contained points from that surface. Figure 1b shows a reproduction of the single triangulated slice which was generated from the MRI image above it in Fig. 1a.

Calculations using the finite element method (FEM) require that the entire region within the surfaces be tessellated into volume elements. We chose to use tetrahedral volume elements due to their relative simplicity and since they are capable of closely following the irregular geometry associated with the human body and the enclosed regions of inhomogeneity. The first step in tetrahedralization of the model was to add internal node points to the previously discretized surface descriptions of each layer. These then became the vertices of the elemental volumes. For this, we devised a "grid-maker", which applied a uniform grid of points to the layer and then excluded those points which were outside the outer surface or too close to any surface in the layer. Once the grid points were defined, all the points from a single slice (two successive layers) were input to a program that connected sets of 4 nodes into volume elements based on three-dimensional Delaunay and Dirichlet criteria for optimal tetrahedra [22, 23]. Figure 1c shows the same slice as in Figs 1a and 1b after it was tetrahedralized in this manner.

Just as the points and triangles from all the slices were combined and sorted to form complete surfaces, so too were the tetrahedralized slices combined to yield the complete geometrical description of the model. Sorting of the tetrahedralized slices also involved keeping track of element connectivities, of links between point in the context of surfaces (triangles) and of the same points as nodes of the volume elements (tetrahedra). Finally, and most importantly, sorting included the determination of conductivity for each element (see next section: "Assignment of conductivity").

Assignment of conductivity

The major advantage of the finite element method is the ability to assign—and easily change—conductivity information for each element of the volume. Hence, it is also possible to include, explicitly, the effect of anisotropy in a finite element solution.

The actual process of determining the value of conductivity for each element in the model consisted of two steps. In the first, the centroid of each tetrahedron was located and projected to the plane defined by the points in the next lower layer. This projected point was then subjected to a sequence of tests in order to determine whether it was inside or outside each surface until finally the location relative to the boundaries was confirmed. The tetrahedral element was then assigned a group number according to the region in which it was found to lie. The actual conductivity values assigned to each element in the second stage of the process was not set until the finite element solution was computed. In this way, it was easy to vary the conductivity without altering the geometrical model.

For all regions except skeletal muscle, a single group number was used. The local nature of muscle fiber orientation, and the resulting change in the conductivity tensor, required that more group numbers be reserved for the muscle region. As a first approximation to the actual fiber orientation, we established 12 muscle regions as wedge-

shaped sectors defined by bounding planes which all intersected at the center line of the torso (the z-axis in this case) and were spaced at regular 30-degree intervals around the thorax as shown in Fig. 2. The slice depicted in Fig. 1c has been color-coded according to the group number, and, thus conductivity values.

The conductivities finally used for each region in the model were based on values from the literature [24]. The muscle regions were assigned conductivities such that the ratio of conductivities—longitudinal vs radial—of the fiber direction was between 3:1 and 5:1, again in accordance with the literature.

Mathematical theory

Electrical activity arising from cardiac sources is governed by Maxwell's equations. It has been shown [18] that for the frequencies of interest in electrocardiography, we can neglect capacitive, inductive, and electromagnetic propagation effects within the volume conductor. This leads to a quasi-static formulation of the field equation (the general form of Poisson's equation for electrical conduction), which can be stated as:

$$\nabla \cdot (\sigma \nabla \Phi) = -I_{SV} \quad \text{in } \Omega \tag{1}$$

with the general boundary conditions:

$$\Phi = \Phi_0 \quad \text{on } \Gamma_E \tag{2}$$

$$(\sigma \nabla \Phi) \cdot \mathbf{n} - g = 0 \quad \text{on } \Gamma_T \tag{3}$$

where:

Φ = potential field
Φ_0 = potentials on the epicardial surface boundary (known *a priori*)
σ = conductivity tensor
I_{SV} = internal current source per unit volume
g = externally applied boundary current (if one exists)
Ω = bounded domain
Γ_E = boundary at the epicardial surface
Γ_T = boundary at the torso surface.

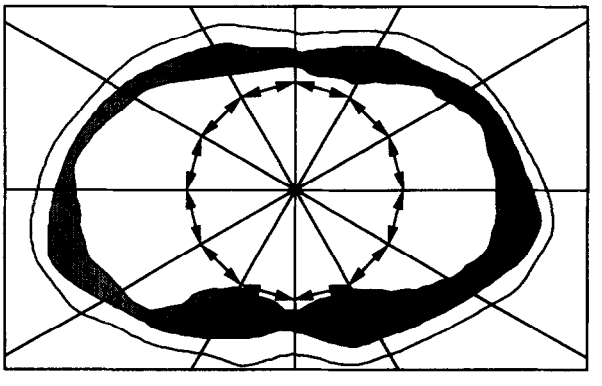

Fig. 2. Diagram of a single slice through the torso model showing the way in which conductivity values were assigned to the anisotropic skeletal muscle. Each transverse torso slice was first divided into 12 equiangular sectors. Muscle fibers were assumed to run in the plane perpendicular to a radial vector drawn from the origin, through the center of each sector. For each tetrahedral volume element whose centroid fell within the sector, the *transverse* value (typically 0.1 S/m) was given to the component of the conductivity tensor in the direction of this ray. All components of the conductivity tensors perpendicular to the radial vector received the *longitudinal* value (typically 0.3 S/m). Orthogonal transformations resolved the tensor components to Cartesian coordinates for use in the finite element calculations.

A solution of (1)–(3) which allows for anisotropy, complex geometries, and inhomogeneities utilizes the finite element method. The finite element method converts the differential equation in (1) according to the principle of virtual work to a more general integral form of the equation which is called the weak formulation of the problem. Since the conductivity tensor is symmetric and Poisson's equation is an elliptical partial differential equation that satisfies the Euler–Lagrange condition for minimization of a functional via the Ritz method of variational calculus, the weak formulation is equivalent to the variational formulation, which, in this case, is also equivalent to the Galerkin formulation [25]. The global integral form over the domain Ω of (1) with boundary conditions (2) and (3) is then:

$$\int_{\Omega} \sigma \nabla \Phi \cdot \nabla \bar{\Phi} \mathrm{d}\Omega = \int_{\Omega} I_{SV} \bar{\Phi} \mathrm{d}\Omega + \int_{\Gamma} g \bar{\Phi} \mathrm{d}\Gamma. \tag{4}$$

Equation (4) holds for an arbitrary continuous function $\bar{\Phi}$ such that $\forall \bar{\Phi} \in \bar{\Phi} = 0$ on Γ_E subject to the condition $\Phi = \Phi_0$ on Γ_E.

Once the equation is in the global integral form, the finite element approximation method can be applied to turn the continuous formulation into an equivalent discrete form. With the discretization completed, one must define the approximation function, i.e. the interpolating function, which solves the discrete form of the equation. The discretization of the potential field and volume conductor was accomplished using isoparametric elements that satisfy the basic convergence requirements for interpolating functions of: smoothness, continuity across the element boundaries, and completeness [25, 26].

In order to apply the interpolation function, all coordinates must be mapped to what is termed the "parent domain", which is a fixed unit coordinate system. The coordinate transformation from the natural coordinates associated with the element parent domain (finite element domain) to the coordinates of a point (x, y, and z location of the mesh points) take place via affine maps. Thus, the elemental volume domain is the image of the biunit cube in the parent domain under a trilinear transformation [25, 26]. The transformations in terms of the elemental coordinates and interpolation functions are:

$$x(\bar{\xi}) = \sum_{a=1}^{8} N_a(\bar{\xi}) x_a^e \tag{5}$$

$$\Phi^h(\bar{\xi}) = \sum_{a=1}^{8} N_a(\bar{\xi}) \Phi^h(x_a^e) \tag{6}$$

where $N_a(\xi, \eta, \zeta) = \frac{1}{8}(1 + \xi_a \xi)(1 + \eta_a \eta)(1 + \zeta_a \zeta)$ is the interpolation function and $\bar{\xi} = |\xi, \eta, \zeta|$ are the natural coordinates (parent domain) in the trilinear hexahedron.

The interpolation function $N_a(\xi, \eta, \zeta)$ originally applies to an eight-node hexahedral element but can be reduced to either a six-node prism or a four-node tetrahedral element by the method of degeneration [25, 26].

The finite element approximation, expressed in terms of the interpolation function, of (1)–(3) is thus:

$$\sum_{e=1}^{E} \bar{\Phi}_a \left(\int_{\Omega^e} \sigma_{ab} \frac{\partial N_a}{\partial x} \frac{\partial N_b}{\partial x} \mathrm{d}\Omega \right) \Phi_b = \sum_{e=1}^{E} \int_{\Omega^e} I_{SV} N_a \bar{\Phi}_s \, \mathrm{d}\Omega + \sum_{e=1}^{E_1} \int_{\Gamma_T^e} g \bar{\Phi}_a N_a \, \mathrm{d}\Gamma \tag{7}$$

where E_1 is the number of elements on Γ_T through which boundary current is applied. The quantity in parentheses is the element stiffness matrix which represents the geometry and conductivity of each finite element. Summation over all the element stiffness matrices yields the global stiffness matrix which contains the geometry and

conductivity of the entire volume conductor. Once the boundary conditions (2) and (3) are applied to (7), the finite element approximation reduces to solving a system of linear equations:

$$\sum_{e=1}^{W} K_{ab}\Phi_a = \sum_{e=1}^{E} I^e_{SVa} + \sum_{e=1}^{E_1} g^e_a \quad \text{with } \Phi = \Phi_0 \text{ on } \Gamma_E \tag{8}$$

where

$$K_{ab} \equiv \int_{\Omega_e} \sigma \frac{\partial N_a}{\partial x}\frac{\partial N_b}{\partial x} d\Omega, \; I^e_{SVa} \equiv \int_{\Omega_e} I_{SV} N_a \bar{\Phi}_a \, d\Omega \text{ and } g^e_a \equiv \int_{\Gamma^e_T} g \bar{\Phi}_a N_a \, d\Gamma.$$

Several different problems of interest in electrocardiography can be solved from the general formulation of (8). If the source current term is zero ($I_{SV}=0$) and the boundary current term is non-zero, effects on the transthoracic currents due to injection of current at the body surface could be computed. Such an injection would provide current equivalent to that introduced by the application of external defibrillation fields. If the externally applied boundary current is zero ($g=0$), and the internal source currents, I_{SV}, are known, then one could calculate the potential and current distributions not only within the thorax, but also on the epicardial surface and through the myocardium. If one excludes all regions containing sources from the domains, one can formulate the problem in terms of a volume bounded by the epicardial and torso surfaces for which Laplace's equation holds. The epicardial potential distribution becomes the necessary and sufficient boundary condition to calculate transthoracic current and potential distributions. This requires solving (8) with the right-hand side equal to zero:

$$\sum_{e=1}^{E} K_{ab}\Phi_a = 0 \quad \text{with } \Phi = \Phi_0 \text{ on } \Gamma_E \tag{9}$$

from which, given the potential field on the epicardial surface, the potentials throughout the thorax and on the body surface can be calculated for any specified conductivity and geometry. Once the thoracic potentials are known, the current density per unit volume can be calculated for each element by approximating the potential gradient and multiplying it by its local conductivity tensor, σ_{ab}.

$$\mathbf{J} = \sum_{e=1}^{E} \sigma_{ab} E_b = \sum_{e=1}^{E} -\sigma_{ab} \nabla \Phi_b. \tag{10}$$

This allows for the calculation of the three-dimensional currents within the thorax that arise due to cardiac electrical activity at any instant of time in the cardiac cycle for which epicardial data exists.

Numerical solution of the finite element approximation

The numerical treatment consists of solving equations (9), for the potential distribution, and (10) for the current density, given different epicardial potential distributions, and for different conductivity configurations. These computations have been previously tested and validated by theoretical studies involving simple geometries and in experimental studies utilizing an electrolytic torso tank [25, 27].

Equation (9) can be solved in several different ways, depending on the further use of the results. For example, if one wishes to calculate solutions to inverse problems then it is necessary to express (9) in terms of a transfer coefficient matrix. The resulting formulation can be used for both forward and inverse solutions:

$$\begin{pmatrix} K_{TT} & K_{TV} & K_{TE} \\ K_{VT} & K_{VV} & K_{VE} \\ K_{ET} & K_{EV} & K_{EE} \end{pmatrix} \begin{pmatrix} \Phi_T \\ \Phi_V \\ \Phi_E \end{pmatrix} = \begin{pmatrix} 0 \\ 0 \\ 0 \end{pmatrix} \text{ with } \Phi = \Phi_0 \text{ on } \Gamma_E \tag{11}$$

or equivalently:

$$\Phi_T = (K_{TT} - K_{TV}K_{VV}^{-1}K_{VT})^{-1}(K_{TV}K_{VV}^{-1}K_{VE} - K_{TE})\Phi_E = A_{TE}\Phi_E. \tag{12}$$

The matrix in (11) is the partitioned global stiffness matrix that expresses the interaction between the various regions of the thorax, where the subscripts T, V, and E stand for torso, volume, and epicardium, respectively. The stiffness matrix is typically very sparse since each element can interact with only a few other neighboring nodes with which there is direct contact. In (12), A_{TE} is the transfer coefficient matrix relating epicardial and torso potentials. Drawbacks of this formulation are primarily computational due to the storage requirements for the various submatrices in (12) and the cost of calculating inverses and performing large matrix multiplications. The advantages are that solutions to (12) are solutions to the forward problem that can also, with some additional manipulations to deal with the ill-conditioned nature of A_{TE} be used to solve the inverse problem. Furthermore, to apply the forward solution to different sets of epicardial potentials requires only a matrix multiplication by A_{TE}.

Other solution methods, which are more commonly used in solving systems of equations that result from finite element approximations, involve manipulating the potential vector and the stiffness matrix in (11) in such a way as to incorporate a single set of boundary conditions and then solve the resulting linear system of equations. The advantages to this approach are typically a significant reduction in memory requirements and solution time, but these are gained at a cost of having to solve (11) again for each set of epicardial potentials. In these methods, boundary conditions are either applied explicitly, changing the corresponding columns of global stiffness matrix to reflect the imposed value at the boundary or by a computationally more efficient way using a penalty method. The penalty method in finite elements works by first adding a large positive value, $C = N \cdot 10^p \cdot \max(K_{ab})$, where N is the order of the system and p is typically $3 \sim 8$, to each diagonal term of the global stiffness matrix that corresponds to a node which has an applied boundary condition, and then multiplying C by the boundary condition and adding it to the right-hand side of equation (9). As long as the value of C is considerably larger than the diagonal elements of the stiffness matrix and the condition number of the stiffness matrix remains within stable limits, the boundary conditions are satisfied to within an error of 10^{-p} [28].

Once the boundary conditions have been applied, one is still left with a potentially large system of linear equations to solve, for which there are a number of techniques. Direct solution methods, while potentially fast, are limited by the size of the system and the amount of available memory, especially when no attempt is made to take advantage of the sparse nature of the stiffness matrix. Iterative methods, on the other hand, are more memory efficient but their performance depends on the number of iterations, and thus the time, required for convergence, if indeed the solution converges at all.

For the solution of this model, we have implemented both direct and iterative solution strategies. In order to improve the performance of direct methods, we made use of a number of storage and program optimizations. The finite element method generates a symmetric, linear system whose computational size is determined by the maximum bandwidth of the global stiffness matrix. The number of non-zero elements along any row (or column) depends on the number of nodes that interact via common elements; therefore, the bandwidth, while potentially small, can become grossly inflated due to an inefficient numbering of the nodes. To reduce this bandwidth, and thus the memory needs for storage of the matrix, we utilized two approaches. The first was a bandwidth optimization algorithm based on that of Cuthill and McKee [29]. This necessitated

reordering the nodes in such a way as to minimize the elemental connectivity, and thus the bandwidth. While this strategy typically reduced the bandwidth by an order of magnitude, it still left numerous zeros in the matrix.

The second, and more successful strategy, involved storing the global stiffness matrix in compressed-sparse-row (CSR) format [30]. According to this scheme, only the non-zero values in the matrix are stored, along with two integer vectors which contain the necessary pointers to locate the original elements. This scheme reduced the storage needs for the global stiffness matrix typically by two orders of magnitude. While such schemes require more overhead to retrieve and store the data, when used with sparse matrix solvers on large (hundreds-of-thousands of elements) problems, the overall effect was a considerable reduction in compute time over direct methods.

Code optimization included, at least for the solvers written in house, use of processor specific basic linear algebra software (BLAS) routines [31–33] for all standard matrix and vector calculations, along with standard Fortran optimization and profiling techniques. Furthermore, we took specific advantage of the super-scalar architecture of the IBM RISC/60000 wherever possible.

Direct solutions consisted of first optimizing the bandwidth, then storing the maximum bandwidth region of the global stiffness matrix in a one-dimensional array, and finally computing the solution using a bandwidth solver based on a modified Gaussian elimination method. The methods for iterative solutions included a Jacobi method with preconditioned conjugate gradients (JCG), successive overrelaxation (SOR), and symmetric SOR with a conjugate gradient preconditioner (SSORCG) [34]. All the iterative methods converged within 500 iterations, with the symmetric SSORCG converging to a stopping criterion of 1×10^{-8} within 250 iterations in the least amount of CPU time.

Data acquisition and experimental procedures

The input data that drive the calculations of the body surface potentials and the thoracic currents are electric potentials from the epicardial surface of the heart. These "electrograms" are gathered as part of clinical procedures performed at the University of Utah Medical Center, for the purpose of determining the location of sources of arrhythmia in patients with chronic cardiac rhythm disturbances that do not respond to less invasive interventions. The standard procedure for such recordings is as follows:

After the chest is surgically opened, but prior to the necessary heart surgery, a 64-electrode recording array is placed in the heart. The array is constructed of 64-enamel insulated, 5 mil diameter, silver wires knotted into nylon stocking material sewn into the basic shape of the heart. The insulation is removed just where the wires are tied into the sock, forming very fine unipolar electrodes.

Electrograms are recorded using a multiplexer consisting of 64 low noise, high input impedance instrumentation amplifiers, each of which is referenced to a Wilson Central Terminal. Each amplifier incorporates a sample and hold circuit to insure simultaneous sampling at rates of 1000 samples per second, and digitized using a 12-bit linear analog to digital to analog converter. Two to fifteen seconds of data are recorded and stored to hard disk for processing.

During processing, the data are gain adjusted and corrected for baseline drift. The data from multiple cardiac cycles can be averaged to further reduce noise and minimize beat to beat variations. Isopotential maps are typically constructed at every 5 msec during the QRS interval and every 20 msec during the ST–T interval, although data are available for every millisecond during the entire QRST interval.

Visualization

In developing the geometrical model and examining the results of simulations, we developed a number of visualization tools specifically for this project. This effort was driven in part by our rather specialized needs, but also by the poor performance of

existing general-purpose programs for scientific visualization. The recent advent of high-powered, dedicated graphics hardware incorporated into the standard UNIX environment, together with mature, well documented, graphics software primitives, made this development both feasible and relatively efficient.

The tools required for this project fell into two overlapping categories: for building and developing the geometric model, we needed interactive, real-time three-dimensional display and editing programs, with which we could view and digitize the MRI images and then examine and alter the resulting points and connectivities. Once data were generated from the model, we needed a second group of programs to visualize the potential distributions and current vector fields in three dimensions, also interactively. Programs in the first category were originally developed in Fortran on the Evans and Sutherland, PS-390, a graphics terminal served by Vax 11/750 and Vax 4000 computers, and then re-written in C for the GL graphics library from Silicon Graphics. We developed the digitizing program used to obtain surface descriptions from the MRI images on the Macintosh II computer in C [21]. The data visualization software was developed exclusively in GL, using both a Silicon Graphics 4D/210 VGX graphics workstation and an IBM RS/6000 workstation equipped with a Silicon Graphics display system.

All programs on the workstations incorporated user input via the keyboard for setting parameters or toggling settings, a mouse for picking objects or editing connectivities, and a dial box for rotating and translating the contents of the display. The models themselves, wire-frame meshes of nodes connected into either triangles or tetrahedra, served as the frame or structure for the display of potentials and currents. From potential data at the vertices of triangular surface elements, we could construct flat and Gouraud shaded, color-coded potential distributions, to which we could then apply scaling, rotation, translation, and clipping planes. For a more quantitative view of the data, construction of color-coded contour lines was often better suited than shaded rendering, especially when combined with different scaling models for the data (linear, exponential, and logarithmic) and different color schemes. Examples of potential displays are shown in Figs 4 and 5.

Display of current vector fields presented some new problems since there are few existing standard methods of displaying data which have both amplitude and directional information, especially in three dimensions [35]. We have included several options in the display graphics, the simplest of which draws for every vector a single "arrow" of normalized length and with the shaft colored according to the vector magnitude. A second form of display requires a starting point to be defined as an element for which the current vector is known. From the centroid of this starting element, a search line is constructed in increments along the direction of the current vector for that element until the endpoint of this line is outside the region enclosed by the entire first-order neighborhood of the starting element. At each increment, the location of the closest element centroid to the interim endpoint is determined and when the search line is finished, the element which was closed overall is selected and a vector drawn to its centroid from the centroid of the starting element. This process continues until the search line hits either an element on the edge of the geometry, or the same element for a second time, yielding a loop which represents a continuous path of current in the volume. The user can then select which and how many such current loops are followed and then display them as continuous, color-coded lines or ribbons. An example of current display is shown in Fig. 5.

RESULTS AND DISCUSSION

Model specifications

For this study, we present two separate models based on a single set of MRI images, one we refer to as the high resolution (H), the other as the medium resolution (M) version. The specifications for both are given in Table 1.

Table 1. Specifications for 2 separate geometric models based on a set of MRI images from a single patient. "H" indicates the high resolution version of the model, "M", the medium resolution version

Surface	No. surface nodes (H/M)	No. triangles (H/M)	Internodal spacing (H/M)	Totals	No. elements (H/M)
Torso	12 000/2867	24 000/5635	5.39/10.99 mm	Surface nodes	42 400/10 711
Fat	11 900/2596	23 600/5077	5.55/11.12 mm	Grid nodes	39 600/11 372
Muscle	11 700/2403	23 200/4684	5.36/10.99 mm	Total nodes	82 000/22 083
Lung	5500/1254	11 000/2321	5.38/11.10 mm	Triangles	84 450/18 676
Epicardial	1591/1591	2650/2650	4.80/4.80 mm	Tetrahedra	500 000/129 946

The terms "high" and "medium" are obviously empirical measures which refer to the ease with which the models could be reasonably managed given our available computational resources. The high resolution version, while enabling us to display and manipulate the geometry, led to a finite element computation which outstripped the memory configurations and CPU capabilities of even the supercomputers at our disposal. In fact, to compute transthoracic currents with the high-resolution version of the model would require at least a week of CPU time and 30 GByte of storage on an IBM 3090/600S supercomputer using our direct-solve algorithms. Partitioning of the problem would reduce the memory requirements at a severe penalty in increased CPU needs. While the medium resolution model contains considerably fewer elements than the high resolution version, it is still twice as large as any other thorax model reported in the literature [36]. Figure 3 shows an anterior view of the complete high-resolution model as a wire mesh diagram. For illustration, each surface is rendered in a different color and a clipping plane has been applied to strip away some of the most anterior triangles.

Simulations

In the first simulations, three sets of artificially generated potentials were used as boundary conditions. Values at the nodes ranged from +20 to −20 mV as a function of their distance from each of three orthogonal planes intersecting at the center of the heart, thus providing simple configurations for testing and illustrative purposes.

The second set of simulations employed epicardial maps recorded during open chest surgery on a human patient. At each instant in time throughout the QRS, the experimentally recorded potentials were mapped to anatomically equivalent positions on the model heart. These potentials then had to be interpolated to yield potentials over the entire ventricular surface of the model heart, which provided the Dirichlet boundary condition for the simulation. Interpolation was performed using a scheme which is equivalent to minimizing a discrete estimation of the Laplacian of the potential over the entire surface of interpolation [37].

To characterize the effect of including anisotropic conductivity within the skeletal muscle on the forward calculation, we computed the intrathoracic potential distribution using both the inhomogeneous isotropic and anisotropic versions of the medium resolution torso model. In the anisotropic model, conductivities were assigned the following values [24]:

subcutaneous fat = 0.045 (S/m)
lungs = 0.096 (S/m)
blood = 0.680 (S/m)
average trunk = 0.240 (S/m)
skeletal muscle = 0.100 (S/m)—perpendicular to fiber orientation
skeletal muscle = 0.300 (S/m)—parallel to fiber orientation,

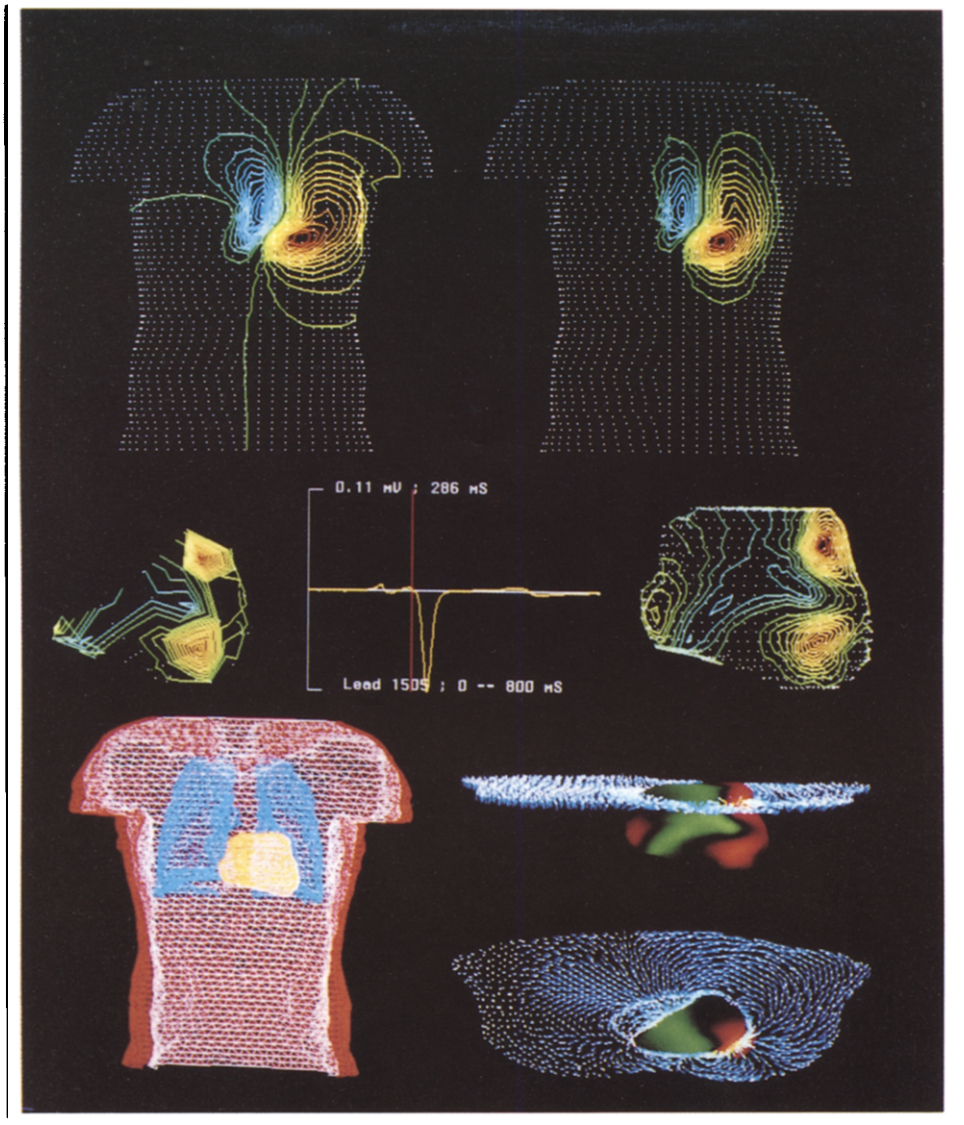

Fig. 3 (Bottom left). The torso, fat, lungs, and epicardial surfaces of the high-resolution torso model shown in an anterior view. Each surface is rendered as a triangularized wire mesh of a different color and a frontal cutting plane has been applied to strip away the most anterior of the triangles.

Fig. 4 (Top and middle). A composite plate of electric potential maps over epicardial and torso surfaces. For each panel we chose the same anterior view and in each map, the equipotential contour lines are color-coded from blue (most negative potential) through green and yellow to red (most positive potential) in linear steps over the range of potential values in the panel. In panel (a) (middle left) is shown the potential distribution derived directly from epicardial potentials measured with a 64-electrode sock from a patient during open-chest arrhythmia surgery. Panel (c) (middle right) depicts the potential distribution over the entire ventricle surface as interpolated from the values in panel (a). Panels (d) and (e) (top left and right) show the body surface potential maps computed using the forward solution. For the results in panel (d) an inhomogeneous, isotropic torso model was used, while for panel (e) the skeletal muscle region was assigned isotropic conductivity values. In panel (b) (middle center) is shown a single, computed ECG tracing from a precordial lead location on the surface of the inhomogeneous, isotropic torso model. The red vertical bar indicates the instant in time at which all the surface maps were taken.

Fig. 5 (Bottom right). Two views of the current vector distribution in a single slice (the same slice as that used in Fig. 1) together with the potential map rendered on the surface of the ventricles at the same instant in time as in Fig. 4. Colors in the potential map are coded from green (most negative), through gray (zero), to red (most positive). Current vectors are depicted as three-dimensional arrows of uniform length with the tip of each colored white and the shaft colored according to the current magnitude (blue for smallest, through yellow and green to red for largest). The upper panel shows an anterior view with approximately 20° of cranial rotation, while the lower panel shows the same transverse slice after 90° of cranial rotation looking inferiorly with the anterior surface of the torso at the bottom of the figure.

Once the potential values were calculated using (9) for all the nodes of the model geometry, potential gradients and then current densities were computed according to equation (10). The results were displayed as potential distributions on all the surfaces of the model and as current density vectors in the volume. The epicardial boundary conditions and the resulting computed body surface potentials for a single instant in time are shown in Fig. 4. Panel 4a shows an equipotential contour map of the measured epicardial potentials and Panel 4c shows the same distribution after it had been interpolated. Panels 4d and 4e contain images of the body surface potential contour maps in the case of the isotropic (4d) and anisotropic (4e) models. In Panel 4b is shown a single calculated ECG lead from the precordial region of the isotropic torso model, the red vertical bar indicates the temporal location at which the potential distributions in Panels 4a, 4c, 4d, and 4e occurred, 34 msec into the QRS.

Comparison of the two epicardial distributions in Fig. 4 confirms the validity of the interpolation procedure—the overall shape of the distribution remains constant while areas of positive and negative potentials remain anchored to the same region of the epicardium. Only over the area not covered by recording electrodes is there slight expansion or shift of potential extrema. The epicardial data used for these calculations were recorded from a patient suffering from Wolff–Parkinson–White syndrome, and this particular beat demonstrates clear signs of pre-excitation via an accessory pathway feeding into the right-ventricular wall. Tell-tale signs include the early, low-amplitude activity in the ECG (delta wave) and the premature activity in the basal, right-ventricular epicardium (green contour lines on the left side of the epicardium).

The resulting computed body surface potential distributions shown in Figs 4d and 4e are typical for the early stage of the QRS. The pre-excitation suggested on the right basal epicardial surface is not yet reflected on the body surface. The dominant feature of the distribution is a pair of positive areas over the left anterior epicardium, which is clearly reflected on the body surface as a precordial maximum. Of interest is the fact that there are two separate areas of positive potential on the epicardial surface that fuse to become a single maximum on the body, documentation of a phenomena long known from experimental studies. The effect of the anisotropic skeletal muscle on the body surface distribution can be seen by comparing the distributions in Figs 4d and 4e. The contour lines in the anisotropic case are more concentrated on the anterior surface than in the isotropic case; in fact, the entire back of the torso is free of contour lines in the anisotropic case, in sharp contrast to the isotropic case. There is also a slight shift in the location of the maxima between the two distributions.

In later frames of the same beat the differences between isotropic and anisotropic body surface distributions become even more marked, drawing what are relatively symmetric and round extrema in the isotropic map into vertically oriented, elliptical regions of positive and negative potential. These effects are not characteristic of recorded body surface maps and are, we feel, an artefact of the manner in which the orientation and degree of anisotropy in the torso model were approximated. While neither the numerical values of 0.1 and 0.3 S/m nor their ratio could be considered inappropriate, the simple manner in which we assigned fiber orientation to the individual volume elements resulted in conductivity tensors which apparently had too strong a cranio-caudal component. This follows directly from our resolution of the fiber direction into transverse components that were always aligned with a ray from the central axis of the body, and longitudinal components that were perpendicular to the same ray, in *all* directions. In reality, the sheets of skeletal muscle that enfold the thorax have longitudinal components that lie more in the transverse plane of the body than we have assumed. Hence the overall effect is an exaggeration of the cranio-caudal component of the skeletal muscle conductivity. Increased longitudinal conductivity will tend to direct the current flow away from the radial direction and hence reduce the amplitude of the body surface potential distribution, concentrating the contour lines where there is significant potential amplitude (anterior surface of the torso) and reducing it altogether in areas which lie further from the heart (posterior surface of the torso).

The computed current field from the same instant in time as depicted in Fig. 4 within a single, transverse slice through the thorax is shown from two different perspectives in Fig. 5a and Fig. 5b. Current flow is indicated by the direction of the arrows; the tips of the vectors are colored white, while the shaft colors range from blue through yellow, green, and then red as a function of the current magnitude. In this figure, current can clearly be seen flowing from the areas of positive potential on the heart surface (colored red) and returning to areas of negative potential (colored green). The magnitude of the current is greatest where flow is directed into the anterior surface of the heart but decreases sharply within a few centimeters of the epicardium. Near the body surface, current is directed parallel to the surface, as dictated by the Neumann boundary condition.

CONCLUSIONS

In this paper we have introduced an inhomogeneous, anisotropic thorax model based on human data for use in electrocardiography with emphasis on the calculation of transthoracic potential and current distributions. The model has utility in a variety of applications in electrocardiography including defibrillation studies, forward and inverse problems, impedance tomography, body surface potential mapping and more generally, to increase the understanding of the general theoretical basis of electrocardiographic waveforms.

We have demonstrated the effects of including the anisotropic skeletal model volume. Since we could detect the influence of anisotropy using the conservative 3:1 estimate of parallel vs perpendicular anisotropy ratios, we predict that a more realistic representation of the anisotropy will produce more pronounced effects. It remains to be seen however, if when a more accurate representation of the layering of the skeletal muscle volume is included, its effect will be to enhance or reduce both the radial current flow and body surface potential amplitudes.

We are presently performing studies which quantitatively measure the effects of specific tissue inhomogeneity and anisotropy on the transthoracic current pathways and to further determine the functional relationships between the discretization level of the geometry and the solution accuracy.

SUMMARY

Electrocardiography has played an important role in the detection and characterization of heart function, both in normal and abnormal states. In this paper we introduce an inhomogeneous, anisotropic thorax model based on human data for use in electrocardiography with emphasis on the calculation of transthoracic potential and current distributions. The model has utility in a variety of applications in electrocardiography including defibrillation studies, forward and inverse problems, impedance tomography, body surface potential mapping and more generally, to increase the understanding of the general theoretical basis of electrocardiographic waveforms.

We have demonstrated the effects of including the anisotropic skeletal model volume in the model. Since we could detect the influence of anisotropy using the conservative 3:1 estimate of parallel vs perpendicular anistropy ratios, we predict that a more realistic representation of the anisotropy will produce more pronounced effects. It remains to be seen however, if when a more accurate representation of the layering of the skeletal muscle volume is included, its effect will be to enhance or to reduce both the radial current flow and body surface potential amplitudes.

We are presently performing studies which quantitatively measure the effects of specific tissue inhomogeneity and anisotropy on the transthoracic current pathways and to further determine the functional relationships between the discretization level of the geometry and the solution accuracy.

Acknowledgements—This research was supported in part by awards from the Nora Eccles Treadwell Foundation and the Richard A. and Nora Eccles Harrison Fund for Cardiovascular Research, NIH Grant HL 42388, by the Heart and Stroke Foundation of Canada, and by a grant for computer time from the Utah Supercomputing Institute, which is funded by the State of Utah and the IBM Corporation.

The authors wish to thank D. Parker for his expertise and assistance in obtaining the MRI data; R. C. Lux for his time, patience, and a body from which to construct our model; T. Oppe, from the Florida Supercomputing Center, and S. Foresti and M. Pernice from the Utah Supercomputer Institute for their comments, suggestions, and CPU cycles; and J. A. Abildskov, K. A. Coles, and R. L. Lux for critiquing our paper and providing valuable suggestions.

REFERENCES

1. D. P. Zipes, J. Fisher and R. M. King, Termination of ventricular fibrillation in dogs by depolarizing a critical amount of myocardium, *Am. J. Cardiol.* **36**, 37 (1975).
2. N. Shibata, P. S. Chen and E. G. Dixon, Epicardial activation after unsuccessful defibrillation shocks in dogs, *Am. J. Physiol.* **255**, H902 (1988).
3. R. A. Crampton, Accepted, controversial and speculative aspects of ventricular defibrillation, *Prog. Cardiovasc. Dis.* **23**, 167 (1980).
4. F. J. Claydon, T. C. Pilkington, A. S. L. Tang, M. N. Morrow and R. E. Ideker, A volume conductor model of the thorax for the study of defibrillation fields, *IEEE Trans. Biomed. Engng* **BME-35**, 1981 (1988).
5. N. G. Sepulveda, J. P. Wikswo and D. S. Echt, Finite element analysis of cardiac defibrillation current distributions, *IEEE Trans. Biomed. Engng* **BME-37**, 354 (1990).
6. M. Ahmed, D. Billie, R. Barker and M. Griesen, Electrical current in the human thorax, *12th Annual International Conference of the IEEE Engineering in Medicine and Biology Society*, p. 642. IEEE Press (1990).
7. R. C. Barr, Genesis of the electrocardiogram, *Comprehensive Electrocardiology*, P. W. Macfarlane and T. D. Veitch Lawrie, Eds, p. 129. Pergamon Press, Oxford, U.K. (1989).
8. B. M. Horacek, Digital model for studies in magnetocardiography, *IEEE Trans. Mag.* **MAG-9**, 440 (1973).
9. R. M. Gulrajani, F. A. Roberge and G. E. Mailloux, The forward problem of electrocardiography, *Comprehensive Electrocardiology*, P. W. Macfarlane and T. D. Veitch Lawrie, Eds, p. 197. Pergamon Press, Oxford, U.K. (1989).
10. R. C. Barr, M. Ramsey and M. S. Spach, Relating epicardial to body surface potentials distributions by means of transfer coefficients based on geometrical measurements, *IEEE Trans. Biomed. Engng* **BME-24**, 1 (1977).
11. P. Colli Franzone, L. Guerri, B. Taccardi and C. Viganotti, Finite element approximation of regularized solution of the inverse potential problem of electrocardiography and applications to experimental data, *Calcolo.* **22**, 91 (1985).
12. C. R. Johnson, The generalized inverse problem in electrocardiography, *12th Annual International Conference of the IEEE Engineering in Medicine and Biology Society*, p. 593. IEEE Press (1990).
13. R. S. MacLeod, Percutaneous transluminal coronary angioplasty as a model of cardiac ischemia: clinical and modelling studies. Ph.D. Thesis, Dalhousie University (1990).
14. B. J. Messinger-Rapport and Y. Rudy, Regularization of the inverse problem: a model study of the effects of geometry and conductivity parameters on the reconstruction of epicardial potentials, *IEEE Trans. Biomed. Engng* **BME-33**, 677 (1986).
15. B. J. Messinger-Rapport and Y. Rudy, Regularization of the inverse problem: a model study, *Math. Biosci.* **89**, 79 (1988).
16. Y. Rudy and R. Plonsey, A comparison of volume conductor and source geometry effects on body surface and epicardial potentials, *Circ. Res.* **46**, 283 (1980).
17. Y. Rudy and B. J. Messinger-Rapport, The inverse problem in electrocardiography: solutions in terms of potentials, *CRC Crit. Rev. Biomed. Engng* **16**, 215 (1988).
18. R. Plonsey, *Bioelectric Phenomena*. McGraw-Hill, New York (1969).
19. R. L.Lux, Mapping techniques, *Comprehensive Electrocardiology*, P. W. Macfarlane and T. D. V. Lawrie, Eds, p. 1001. Pergamon Press, New York (1989).
20. L. S. Green *et al.*, Effects of age, sex, and body habitus on WRS and ST-T potential maps of 1100 normal subjects, *Circulation* **71**, 244 (1985).
21. P. R. Ershler, R. L. Lux, L. S. Green, G. R. Caputo and D. Parker, Determination of three-dimensional torso, heart and electrode geometries from magnetic resonance images, *10th Annual International Conference of the IEEE Engineering in Medicine and Biology Society*, p. 121. IEEE Press (1988).
22. A. Bowker, Computing Dirichlet tesselations, *Computer J.* **24**, 162 (1981).
23. C. L. Lawson, Software for C1 surface interpolation, *Mathematical Software II*, J. R. Rice, Ed., p. 161. Academic Press, New York (1977).
24. K. R. Foster and H. P. Schwan, Dielectric properties of tissue and biological materials: A critical reveiw, *CRC Crit. Rev. Biomed. Engng* **17**, 25 (1989).
25. C. R. Johnson, The generalized inverse problem in electrocardiography: Theoretical, computational, and experimental results. Ph.D. Thesis, University of Utah (1990).
26. T. Hughes, *The Finite Element Method: Linear Static and Dynamic Finite Element Analysis*. Prentice Hall, NJ (1987).
27. C. R. Johnson and A. E. Pollard, Electrical activation of the heart: computational studies of the forward and inverse problems in electrocardiography, *Computer Assisted Analysis and Modeling*, p. 583. MIT Press, Boston (1990).
28. H. Kardestuncer, *Finite Element Handbook*. McGraw-Hill, New York (1985).

29. E. Cuthill and J. McKee, Reducing the bandwidth of sparse symmetric matrices, *ACM Proc. of 24th natn. Conf.* (1969).
30. I. S. Duff, A. M. Erisman and J. K. Reid, *Direct Methods for Sparse Matrices*. Clarendon Press, Oxford (1986).
31. C. L. Lawson, R. J. Hanson, D. R. Kincaid and F. T. Krogh, Basic linear algebra subprograms for Fortran usage, *ACM Trans. Math. Soft.* **5**, 3087 (1979).
32. J. J. Dongarra, J. Du Croz, S. Hammarling and R. J. Hanson, An extended set of FORTRAN basic linear algebra subprograms, *ACM Trans. Math. Soft.* **14**, 1 (1988).
33. J. J. Dongarra, J. Du Croz, S. Hammarling and I. Duff, A set of level 3 basic linear algebra subprograms, *ACM Trans. Math. Soft.* **16**, 1 (1990).
34. D. Kincaid, Acceleration parameters for a symmetric successive overrelaxation conjugate gradient method for symmetric systems, *Advances in Computer Methods for Partial Differential Equations*, R. Vichnevetsky and R. Stepleman, Eds, p. 294. IMACS (1981).
35. J. L. Helman and L. Hesselink, Visualizing vector field topology in fluid flow, *IEEE Comput. Graph. Appl.* **11**, 36 (1991).
36. A. S. Vahid and P. Savard, A volume conductor model of the human thorax for field calculations, *12th Annual International Conference of the IEEE Engineering in Medicine and Biology Society*, p. 615. IEEE Press (1990).
37. T. F. Oostendorp, A. van Oosterom and G. Huiskamp, Interpolation on a triangulated 3D surface, *J. Comput. Phys.* **80**, 331 (1989).

APPENDIX. SOFTWARE DEVELOPMENT

This Appendix contains a list and short explanations of the original software developed for the construction and use of the CVRTI Torso model.

(1) *mri2ps*	Converts MRI image data into postscript files.
(2) *new_digitizer*	Manually selects pixels (x, y coordinates) from each MRI slice (Macintosh II).
(3) *mri_metric*	Scales, shifts, and sorts the digitized surface points from the MRI images.
(4) *mri_spline*	Uses a parametric cubic spline to smooth raw data points into evenly spaced points on a contour.
(5) *mri_tri*	Automatically triangulates a pair of MRI contour layers.
(6) *tri_sort*	Sorts triangulated slices into complete surface descriptions.
(7) *mri_point_adder*	Automatically produces a grid of points based upon a minimum separation distance criterion.
(8) *tessellate*	Tetrahedralizes a cloud of points in three dimensions.
(9) *tetra_tester*	Tests the tetrahedra, generated by *tessellate*, according to minimum volume and length criteria, and deletes tetrahedra that were formed outside the boundary in convex regions.
(10) *tetra_sort*	Sorts tetrahedralized slices into complete volume descriptions, including determination of conductivity for each element.
(11) *edtri*	Displays points, surfaces and volumes for interactive editing of connectivities.
(12) *cjmaps*	Interactively visualizes and displays the model geometry, rendered potential distributions, contour maps, and current vector fields.
(13) *ecgfe3D*	Solves Poisson's (and Laplace's) equation using a general three-dimensional finite element algorithm with options for a variety of different boundary conditions.

About the Author—CHRISTOPHER R. JOHNSON received the B.S. degree in Physics from Wright State University, Dayton, Ohio, and the M.S. degree in Physics and the Ph.D. degree in Biophysics from the University of Utah, Salt Lake City, UT. Dr Johnson is currently a Research Assistant Professor of Computer Science as well as an Adjunct Assistant Professor in the Departments of Bioengineering and Mathematics at the University of Utah, Salt Lake City, UT. His current research interests include mathematical modeling of physiological systems as it pertains to theoretical electrocardiology, forward and inverse problems, supercomputing and visualization in medicine, and the applications of non-linear dynamical systems in medicine and biology.

About the Author—ROBERT S. MACLEOD received his B.Sc. degree in Engineering Physics from Dalhousie University, Halifax, N.S., M.Sc. degree in Electrical Engineering from the Technische Universität Graz, Austria, and Ph.D. degree in Physiology and Biophysics from Dalhousie University, Halifax, N.S. Dr MacLeod is currently a Research Associate in Internal Medicine at the Nora Eccles Harrison Cardiovascular Research and Training Institute at the University of Utah. His research interests include forward and inverse problems, computational electrophysiology, body surface potential mapping, and visualization in medicine.

About the Author—PHILIP R. ERSHLER received the B.A. degree in Mathematics from Colorado College in 1972. He received the M.S. and Ph.D. degrees in Electrical Engineering from the University of Utah in 1975 and 1986, respectively. He has been associated with the Nora Eccles Harrison Cardiovascular Research and Training Institute at the University of Utah since 1973. In 1986 he received a faculty appointment as Assistant Research Professor in Internal Medicine. His research interests have centered around real-time computer data acquisition and processing and computer graphics as applied to electrophysiologic research.